Optimization of surface coating on Fe3O4 nanoparticles for high performance magnetic hyperthermia agents

ARTICLE *in* JOURNAL OF MATERIALS CHEMISTRY · APRIL 2012

Impact Factor: 7.44 · DOI: 10.1039/C2JM30472D

8 AUTHORS, INCLUDING:

Xiaoli Liu
National University of Singapore
31 PUBLICATIONS **205** CITATIONS
SEE PROFILE

Hai-Ming Fan
Northwest University
80 PUBLICATIONS **2,331** CITATIONS
SEE PROFILE

Jiabao Yi
University of New South Wales
126 PUBLICATIONS **3,190** CITATIONS
SEE PROFILE

Eugene Shi Guang Choo
National University of Singapore
20 PUBLICATIONS **566** CITATIONS
SEE PROFILE

Journal of Materials Chemistry

Cite this: DOI: 10.1039/c2jm30472d

www.rsc.org/materials

PAPER

Optimization of surface coating on Fe_3O_4 nanoparticles for high performance magnetic hyperthermia agents†

Xiao Li Liu,[ab] Hai Ming Fan,*[a] Jia Bao Yi,[c] Yang Yang,[b] Eugene Shi Guang Choo,[b] Jun Min Xue,[b] Dai Di Fan[a] and Jun Ding*[b]

Received 24th January 2012, Accepted 29th February 2012
DOI: 10.1039/c2jm30472d

Highly monodispersed magnetite nanoparticles with controlled particle size and mPEG surface coating have been successfully synthesized as a model system to investigate the effect of surface coating on the specific absorption rate (SAR) under an alternating magnetic field. Enhanced SAR with decreased surface coating thickness was observed and ascribed to the increased Brownian loss, improved thermal conductivity as well as improved dispersibility. By elaborate optimization of the surface coating and particle size, a significant increase of SAR (up to 74%) could be achieved with a minimal variation of the saturation magnetization (<5%). In particular, the 19nm@2000 sample exhibited the highest SAR of 930 W g^{-1} among the samples. Furthermore, this high heating capacity can be maintained in various simulated physiological conditions. Our results provide a general strategy for surface coating optimization of magnetic cores for high performance hyperthermia agents.

Introduction

Magnetic nanoparticles offer unique size and shape tunable physical properties that have attracted significant interest for various biomedical applications such as biosensors, magnetic resonance imaging (MRI), magneto-infection, and drug delivery.[1–8] In particular, magnetic nanoparticles like magnetite have shown an intriguing ability to mediate a high rate of heat induction at low concentrations as compared to their bulk counterpart.[9] Application of an external alternating magnetic field (AMF) on magnetic nanoparticles evokes magnetization reversal, and production of thermal energy is continuously measured in terms of the specific absorption rate (SAR) as the nanoparticles return to their relaxed states.[10–12] The conversion of electromagnetic energy into heat by magnetic nanoparticles has great potential as a non-invasive and powerful therapy technique for biomedical applications. For example, magnetic fluid hyperthermia (MFH) can be used to generate localized heating for tumor repression. By targeting the magnetic nanoparticles at the tumor site with an applied AMF, the temperature at tumor sites can be increased to 42–46 °C, which largely reduces the viability of cancer cells.[13–15] In addition, the advancements in functionalization of magnetic nanoparticles enable such therapeutic treatments to selectively kill cancer cells by localized heating, without having to limit the extent of tissue penetration. Thus, the therapeutic efficacy is greatly enhanced compared to conventional chemotherapy and radiotherapy. Magnetic nanoparticle-based hyperthermia agents can also be utilized for controlled delivery of drugs as well as combination with MR imaging at the cellular and molecular level, making magnetic nanoparticle-based hyperthermia agents a promising material for multimodal diagnosis and treatment of a number of diseases.[8,16] However, the relatively poor SAR of current hyperthermia agents, attributed to either low saturation magnetization from small particle sizes or agglomeration of nanoparticles due to inappropriate surface coating, hinders their practical application.[17,18] In this context, the development of a novel hyperthermia agent with both high biocompatibility and high heat transfer efficiency is of utmost importance for the application of magnetic hyperthermia.

Previous studies have focused on designing and optimizing the size, composition and structure of magnetic nanoparticles to maximize the SAR of MFH.[17,19–25] Ma *et al.* found that magnetite nanoparticles with a size of 46 nm exhibited the highest SAR, whereas Hergt *et al.* reported the highest SAR for 30 nm magnetite nanoparticle suspensions.[17,22] The size distribution of nanoparticles has a crucial influence on the SAR, where monodispersed magnetic nanoparticles show a larger SAR than polydispersed magnetite nanoparticles due to the decrease in the proportion of particles contributing to total heat generation in

[a]*Shaanxi Key Laboratory of Degradable Biomedical Materials, School of Chemical Engineering, Northwest University, Xi'an, Shaanxi 710069, China. E-mail: nanofhm@gmail.com*
[b]*Department of Materials Science & Engineering, Faculty of Engineering, National University of Singapore, 7 Engineering Drive 1, Singapore 117574. E-mail: msedingj@nus.edu.sg*
[c]*School of Materials Science and Engineering, University of New South Wales, Kensington, NSW, 2052, Australia*
† Electronic supplementary information (ESI) available: The measured saturation magnetization, coercivity and remanence of the samples. See DOI: 10.1039/c2jm30472d

polydispersed samples.[23,24] Very recently it was discovered that by tuning the exchange coupling between a magnetically hard core and magnetically soft shell, core–shell magnetic nanoparticles can attain a specific loss power one order of magnitude larger than conventional iron oxide nanoparticles.[25] Other than the effect from the intrinsic nature of the inorganic component, a useful approach to improve the performance of magnetic nanoparticles in biomedical applications is the optimization of the surface coating. For instance, high T_2 relaxivity in MRI could be achieved by coating the surface of Fe_3O_4 nanoparticles with 1,2-distearoyl-sn-glycero-3-phosphoethanolamine-*N*-[methoxy(poly ethylene glycol)].[26] Hence, it can be seen that the surface coating plays an important role in colloidal stability, biocompatibility, surface properties, hydrodynamic volume and the viscosity of the magnetic fluid that eventually alters the performance of the MFH agent. So far various biocompatible polymers or macromolecules have been used for the surface modification of magnetic nanoparticles.[17,22,27] However, conflicting SAR values obtained for a certain sized nanoparticle makes it difficult to evaluate the exact contributions of surface coating on the SAR. Furthermore, it is still an unmet challenge to optimize surface coating of magnetic nanoparticles so that they possess not only high thermal efficiency as heating elements but also high biocompatibility and colloidal stability in aqueous solution. Hence, it is imperative to design magnetic nanoparticles with specifically tailored surface chemistry to address the pending needs of MFH related applications.

In the present study, a series of highly monodisperse phosphorylated methoxy poly (ethylene glycol) (mPEG) coated magnetite (Fe_3O_4) nanoparticles have been prepared and employed as a model system to investigate the effect of surface coating on SAR. Both Fe_3O_4 and mPEG were chosen in this work because of their excellent biocompatibility. The sizes of Fe_3O_4 magnetic cores are tuned from 9 to 31 nm in diameter while their surfaces are coated with phosphorylated mPEG of molecular weights ranging from 2000 to 20 000. The crystal structure, morphology and magnetic properties of mPEG coated Fe_3O_4 nanoparticles as well as the colloidal stability of the dispersions are characterized. The dependence of the measured SAR on the surface coating for different sized Fe_3O_4 nanoparticles is systematically investigated. The optimized hyperthermia agents have been further examined in simulated physiological environments with protein (bovine serum albumin, BSA), blood sugar (dextrose), electrolytes (saline) and phosphate buffered saline (PBS). The goal of this study is to gain insight into the intricate interplay of particle size, magnetic properties, colloidal stability and surface coating on the effect on the SAR as well as provide a general strategy to optimize the surface coating of magnetic nanoparticle for high performance hyperthermia agents in biomedical applications.

Experimental

Materials

Methoxy poly(ethylene glycol) (mPEG; $M_w = 2000$ Da, 5000 Da, and 20 000 Da), benzyl ether (99%), tetrahydrofuran (THF; 99.9%), BSA and glucose were obtained from Aldrich. Iron(III) acetylacetonate ($Fe(acac)_3$; 97.9%) and oleic acid were purchased from Fluka. Hexane (J.T. Baker, 99.0%) and chloroform (Fisher Scientific; 99.99%) were used as received.

Preparation of magnetic Fe_3O_4 nanoparticles

Fe_3O_4 nanoparticles were prepared by a well-established solution-phase thermal decomposition method.[28] In a typical synthesis of 19 nm Fe_3O_4 nanoparticles, iron(III) acetylacetonate (12 mmol) and oleic acid (40 mmol) were added to benzyl ether (50 mL) and magnetically stirred under a flow of nitrogen for 30 min. The reaction mixture was slowly heated to 165 °C for 30 min and then heated to 280 °C to reflux for another 30 min under a nitrogen atmosphere. The black–brown mixture was cooled down to room temperature after the reaction. Under ambient conditions, ethanol (30 mL) was added to the mixture, and the product of Fe_3O_4 nanoparticles were separated *via* centrifugation. The particle size was tuned by varying the heating temperature and reaction time.

Preparation of phosphorylated mPEG coated Fe_3O_4 nanoparticles

The hydrophobic Fe_3O_4 nanoparticles were transferred to a water phase *via* a ligand exchange reaction whereby phosphorylated mPEG displaces oleic acid as surfactant. Phosphorylated mPEG was obtained by reacting $POCl_3$ with mPEG as previously described.[29] In a typical process, Fe_3O_4 nanoparticles (5 mg) were transferred into chloroform (20 mL), followed by the addition of phosphorylated mPEG (50 mg; $M_w = 2000$ Da). The mixture was then shaken for 2 h under ambient conditions. After the reaction was complete, the solvent was evaporated under a flow of argon and then dried in vacuum for 2 days to obtain a completely dried nanoparticle powder. The dried nanoparticles were then dispersed into water (5 mL) and the solution was centrifuged at 3000 rpm for 10 min. The supernatant was collected and stored for future use. The same procedure was used to coat different sized Fe_3O_4 nanoparticles using phosphorylated mPEG of different molecular weights ranging from 2000 Da to 20 000 Da. The samples with different sizes and coated with phosphorylated mPEG are labeled in the form of particle size@molecular weight of mPEG (*e.g.* 9nm@2000 and 31nm@5000).

Characterization

The crystal phase of the as-prepared Fe_3O_4 nanoparticles was determined by powder X-ray diffractometry (Bruker D8 Advanced Diffractometer System) with a Cu K_a (1.5418 Å) source. The particle size and morphology of the phosphorylated mPEG coated Fe_3O_4 nanoparticles were examined using transmission electron microscopy (TEM, JEOL 100CX) at an acceleration voltage of 200 kV. The corresponding particle size distribution was obtained by measuring the average diameters of 150–200 nanoparticles. UV–Vis absorption spectra were taken using a Shimadzu UV-1601 UV–Visible spectrophotometer. FT-IR spectra were measured using a Varian 3100 FT-IR (Excalibur series) spectrophotometer. The hydrodynamic diameters and zeta potentials of the nanoparticles were measured using a Malvern Zetasizer Nano-ZS. Samples were equilibrated at 25 °C for 1 min before the measurements and 5 sets of

measurements were taken. The samples magnetic properties were characterized by a LakeShore Model 7407 vibrating sample magnetometer (VSM).

SAR measurements

In principle, a magnetic material subjected to AMF produces a volumetric power dissipation P, and is measured in terms of specific absorption rate (SAR),[30] as given by

$$\mathrm{SAR} = \frac{P}{\rho} = \pi\mu_0\chi_0 H_0^2 f \frac{1}{\rho} \quad (1)$$

where SAR is expressed as W g^{-1} of Fe, $\mu_0 = 4\pi \times 10^{-7}$ N A^{-2} is the permeability of free space, $H_0^2(\mathrm{Am}^{-1})$ is the magnetic field intensity in the material, ρ is the density of the magnetic material, f is the field frequency and χ'' is the imaginary component of complex susceptibility. The imaginary susceptibility of magnetic nanoparticles is given by:

$$\chi'' = \mu_0 M_s^2 V \frac{\omega\tau}{k_B T\left[1 + (\omega\tau)^2\right]} \quad (2)$$

where M_s is the saturation magnetization of the magnetic nanoparticles, V is the volume of the spherical nanoparticle, $\omega = 2\pi f$ is the angular frequency of the AMF, k_B is the Boltzmann constant, and T is temperature. Substituting (2) into (1) yields an approximate expression of the SAR for a finite-size nanoparticle without any surface coating.

$$\mathrm{SAR} = \frac{8\pi^3\mu_0^2 M_s^2 r^3 H_0^2 f^2 \tau}{3\rho k_B T(1 + 2\pi f\tau)^2} \quad (3)$$

The induction heating of magnetic fluids is mainly from the Brownian–Néel relaxation loss of a finite-size sample. In Brownian relaxation, the magnetic moment of a magnetic nanoparticle is locked to the crystal axis and aligns with the external field. When subjected to an AMF, the particle moment rotates as well. While in Néel relaxation, the magnetic moment rotates within the crystal with the applied magnetic field. The Brownian and Néel relaxation times are given by

$$\tau_B = \frac{3\eta V}{k_B T} \quad (4)$$

$$\tau_N = \tau_0 \exp\frac{KV}{k_B T} \quad (5)$$

where η is medium viscosity. As for a finite-size sample system, Brownian and Néel processes take place in parallel, and the effective relaxation time τ is thus given by

$$\frac{1}{\tau} = \frac{1}{\tau_B} + \frac{1}{\tau_N} \quad (6)$$

For experimental determination of SAR, the magnetic nanoparticle dispersions were placed into a Cu coil. Temperature changes against the time of exposure to an AMF (amplitude, 27 kA m^{-1}; frequency, 400 kHz) were recorded with the software provided by the equipment (Ambrell, Easy Heat 4.2–10 kW) using an optical fiber connected to a multimeter. The SAR is obtained using the equation:

$$\mathrm{SAR} = C\frac{\Delta T}{\Delta t}\frac{1}{m_{Fe}} \quad (7)$$

where C is the specific heat of the medium (C_{water} = 4.18 J g^{-1} $°C^{-1}$), $\Delta T/\Delta t$ is the initial slope of the time-dependent temperature curve and m_{Fe} is the weight fraction of Fe in the medium.[31] Iron concentrations of samples were determined by ICP-OES analysis using a Perkin-Elmer Dualview Optima 5300 DV ICP-OES system.

The influence of simulated physiological conditions, such as protein (bovine serum albumin, 0–10%), blood sugar (glucose, 0–1000 mg L^{-1}), electrolytes (saline, containing NaCl 150 mM) and PBS (pH 7.4) for studying the chemical effects on the heating capacity of magnetic nanoparticles was also investigated at a sample concentration of 0.5 mg mL^{-1} under AMF (amplitude, 27 kA m^{-1}; frequency, 400 kHz).

Results and discussions

Synthesis of water-stable Fe_3O_4 nanoparticles

High quality monodispersed Fe_3O_4 nanoparticles were synthesized by the well-established solution-phase thermal decomposition of iron acetylacetonate. The size of the Fe_3O_4 nanoparticles was tuned by controlling the growth temperature and reaction time. Compared to a low temperature water-phase synthetic approach, this approach ensures the high quality of the obtained Fe_3O_4 nanoparticles. Their narrow size distribution and good crystallization could serve as a model system for determining the effect of surface coating in magnetic hyperthermia measurements. The as-prepared Fe_3O_4 nanoparticles are hydrophobic due to oleic acid immobilized on the surface of Fe_3O_4 nanoparticles *via* carboxylic acid groups. In order to transfer these nanoparticles into a water phase, the surface ligands are replaced by phosphorylated mPEG. Fig. 1 schematically illustrates the ligand exchange process on the surface of Fe_3O_4 nanoparticles. Since the phosphate is a strong ligand of Fe,[29,32] the phosphorylated mPEG can readily replace the oleic acid on the surface of Fe_3O_4 nanoparticles at room temperature without any significant change in their size and monodispersity. It is worth noting that both Fe_3O_4 and phosphorylated mPEG have high biocompatibility and flexibility for future biomedical applications.[26]

Structure and surface characterization

The crystal structures of the as-prepared Fe_3O_4 nanoparticles were examined using X-ray diffraction (XRD). Fig. 2 shows the XRD patterns of different sized Fe_3O_4 nanoparticles. All diffraction peaks can be exclusively indexed as cubic spinel Fe_3O_4 (JCPDS no. 19-0629) and no other impurities are observed. The

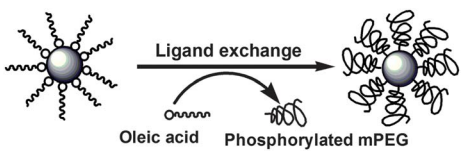

Fig. 1 Schematic diagram illustrating the surface coating of phosphorylated mPEG on Fe_3O_4 nanoparticles *via* ligand exchange.

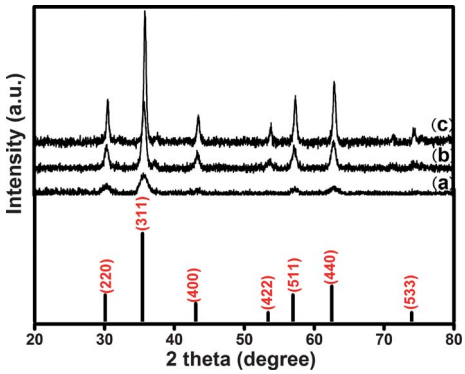

Fig. 2 XRD patterns of Fe_3O_4 nanoparticles. (a) 9 nm Fe_3O_4 nanoparticles, (b) 19 nm Fe_3O_4 nanoparticles and (c) 31 nm Fe_3O_4 nanoparticles.

broadening of XRD peaks due to the small particle size was observed. TEM images of different sized Fe_3O_4 coated by phosphorylated mPEG ($M_w = 5000$ Da) are shown in Fig. 3. As shown in Fig. 3(a–c), these Fe_3O_4 nanoparticles have uniform size and shape after surface modification and no appreciable agglomeration such as dimers and trimers are observed. The average size of Fe_3O_4 nanoparticles are 9 nm, 19 nm and 31 nm, respectively. They are identical to that of the as-prepared Fe_3O_4 nanoparticles estimated using both Scherrer's equation and TEM analysis, indicating that the surface modification of phosphorylated mPEG does not change the structure and morphology of Fe_3O_4 nanoparticles. In addition, the size histograms shown on the right of Fig. 3 reveal the narrow size distribution of Fe_3O_4 nanoparticles. The successful phase transfer could be also seen by the optical images in the inset of Fig. 3, which show the stable aqueous dispersions of phosphorylated mPEG coated Fe_3O_4.

The phosphorylated mPEG coated Fe_3O_4 nanoparticles were further characterized by UV–Vis absorbance and FT-IR spectroscopy to verify the formation of phosphorylated mPEG coating. Fig. 4a shows the UV–Vis absorption spectra of phosphorylated mPEG and Fe_3O_4 nanoparticles before and after the ligand exchange reaction. The absorption band at 255 nm, which is attributed to the phosphate group of phosphorylated mPEG,[33] is present in modified Fe_3O_4 nanoparticles but absent in unmodified Fe_3O_4 nanoparticles. This implies that the phosphorylated mPEG instead of oleic acid was capped on the surface of Fe_3O_4 nanoparticles. More evidence of the capping of phosphorylated mPEG on Fe_3O_4 was found using FT-IR spectroscopy. As shown in Fig. 4b, oleic acid coated Fe_3O_4 nanoparticles exhibit a metal–oxygen band, ν_1, at 590 cm^{-1}, which corresponds to the intrinsic stretching vibrations of the metal at a tetrahedral

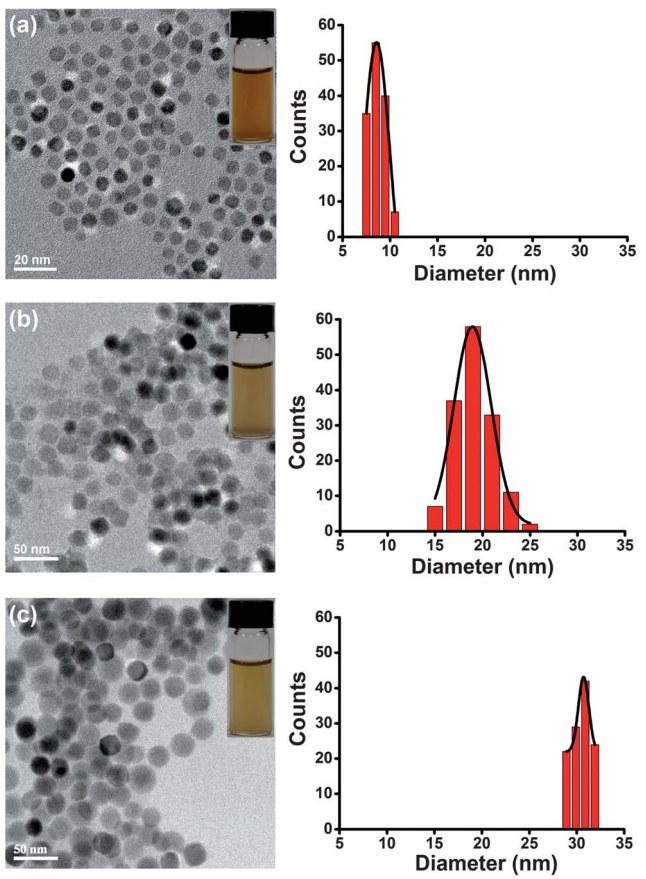

Fig. 3 TEM images of Fe_3O_4 nanoparticles with different sizes. (a) 9 nm Fe_3O_4 nanoparticles, (b) 19 nm Fe_3O_4 nanoparticles, (c) 31 nm Fe_3O_4 nanoparticles, dispersed in water by coating of mPEG 5000. The insets are the digital photographs of Fe_3O_4 nanoparticles dispersed in aqueous solution. The histograms on the right are the corresponding size distributions.

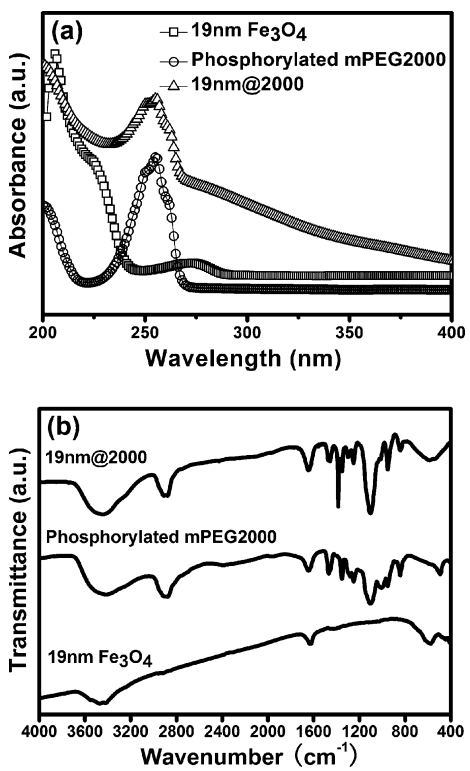

Fig. 4 (a) UV absorbance of Fe_3O_4 nanoparticles before ligand exchange (□), phosphorylated mPEG 2000 (○) and Fe_3O_4 nanoparticles after ligand exchange (△); (b) FT-IR spectra of Fe_3O_4 nanoparticles before ligand exchange, phosphorylated mPEG 2000 and Fe_3O_4 nanoparticles after ligand exchange.

site (Fe_{tetra} ↔ O).[34] It also shows a relevant vibrational band at 1630 cm^{-1} that is characteristic of the asymmetric and symmetric COO^- vibration of the chelating bidentate interaction between oleic acid and Fe ions on the surface of the Fe_3O_4 nanoparticles.[35] In the FT-IR spectrum of phosphorylated mPEG, the asymmetric stretching vibration (ν_{as} (COC)) of the methacryloyloxy group at 1101 cm^{-1},[36,37] asymmetric CH_2 stretching vibrations at 2910 cm^{-1},[38] stretching vibrations of hydroxyl at 3480 cm^{-1},[37] and coupled vibration band of P–O stretching vibration at 1003 cm^{-1}[39,40] are observed. As for phosphorylated mPEG modified Fe_3O_4 nanoparticles, the asymmetric CH_2 stretching vibrations slightly shift to 2875 cm^{-1}. A sharp peak at 584 cm^{-1} appears and it could be attributed to the metal–oxygen bond. Other characteristic bands such as the bands at 1645, 1466, 1298, 1244, 951, and 837 cm^{-1} are also observed for modified Fe_3O_4 nanoparticles. These observations clearly indicate the presence of phosphorylated mPEG on the surface of Fe_3O_4 nanoparticles after ligand exchange.

Magnetic properties characterizations

The magnetic properties of the Fe_3O_4 nanoparticles were characterized using a VSM at room temperature. Fig. 5(a–c) show the hysteresis loops of different sized Fe_3O_4 nanoparticles before and after surface modification. Magnified hysteresis loops are presented in Fig. 5d. The saturation magnetizations (M_s), coercivities and remanences of all samples are summarized in Table S1.† As shown in Fig. 5a, the 9 nm Fe_3O_4 nanoparticles (both unmodified and modified) showed no remanence (H_r) or coercivity (H_c) at room temperature, indicating superparamagnetic behavior. However, the M_s shows a clear drop after surface modification from 57 to 51 emu g^{-1}, to 46 emu g^{-1} with increasing polymer chain length, which is attributed to the reduced effective weight fraction of magnetic core. In contrast, both 19 nm and 31 nm Fe_3O_4 nanoparticles show small H_r and H_c values, which are 2.19 emu g^{-1} and 5.10 Oe for 19 nm, and 7.24 emu g^{-1} and 22.21 Oe for 31 nm, respectively, indicating ferromagnetic-like behavior at room temperature. Similar to the results found for 9 nm Fe_3O_4 nanoparticles, the M_s sharply decreases after surface modification and further decreases with increasing chain length of polymer for both 19 nm and 31 nm Fe_3O_4 nanoparticles. In addition, the reduced M_s with decreasing size is observed for Fe_3O_4 nanoparticles due to the finite size effect.[41] The variation of M_s for a certain sized nanoparticle with respect to different polymer chain lengths is within 10% and this value tends to be smaller with increasing particle size (less than 3% for 31 nm Fe_3O_4 nanoparticles). Such small variations suggest that the chain length of the coated polymer does not significantly change the magnetic properties.

The magnetic properties of the nanoparticles have a strong correlation with the magnetic hyperthermia effect. In a finite-size nanoparticle system, the heat generated by magnetic fluids under an AMF is mainly attributed to two relaxation losses: Néel and Brownian relaxations. Heat generation through Néel relaxation is due to rapidly occurring changes in the direction of magnetic moments relative to the crystal lattice (internal dynamics). This is hindered by the energy of anisotropy that tends to orient the magnetic domain in a given direction relative to the crystal lattice. Brownian relaxation is attributed to physical rotation of particles within a medium in which they are placed (external dynamics) and is hindered by the viscosity, which tends to counter the movement of particles in the medium.[42] Generally,

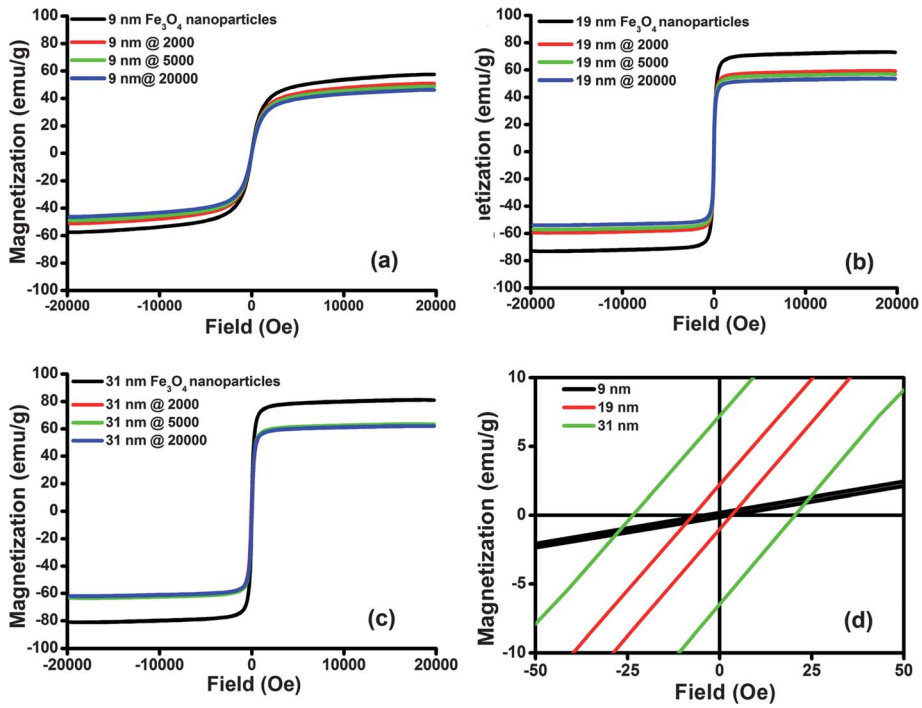

Fig. 5 Magnetic hysteresis loops of Fe_3O_4 nanoparticles of sizes (a) 9 nm Fe_3O_4 nanoparticles; (b) 19 nm Fe_3O_4 nanoparticles; and (c) 31 nm Fe_3O_4 nanoparticles, which are coated with oleic acid (black), mPEG2000 (red), mPEG5000 (green), and mPEG20 000 (blue). (d) The magnified hysteresis loops are of different sized Fe_3O_4 nanoparticles with an oleic acid coating: 9 nm (black), 19 nm (red) and, 31 nm (green).

for a certain magnetic nanoparticle the measured SAR depends on the parameters of magnetic nanoparticles (size, shape, crystal structure, saturation magnetization, and magnetic susceptibility) as well as field strength (H) and frequency (f) of the AMF, according to the description in eqn (3). At a fixed external AMF, the nanoparticles with high M_s will lead to a high SAR. Since M_s decreases as the size decreased, the 9 nm sample with the smallest M_s are expected to exhibit the smallest SAR. Moreover, as only small variation in M_s was observed for a Fe_3O_4 nanoparticles coated with different molecular weights, any significant change in the measured SAR should be due to the factors other than its intrinsic magnetic properties.

Colloidal stability of phosphorylated mPEG coated Fe_3O_4 nanoparticles

Since the dispersibility and colloidal stability of MFH plays an important role in magnetic hyperthermia treatment, the stability of the modified Fe_3O_4 with different sizes and varied mPEG coatings were examined using dynamic light scattering (DLS). Fig. 6 shows the hydrodynamic sizes of all samples with different polymer chain lengths. The average sizes of the samples are summarized in Table 1. The measured hydrodynamic sizes in aqueous solution are slightly larger than that of TEM observations. This provides additional evidence for the existence of the polymer coating on the nanoparticles and these sizes are within the appropriate size range for biomedical applications.[43] For most samples, the hydrodynamic size increased as the particle size and the length of the polymer increased. However, for the 31 nm Fe_3O_4 nanoparticles, the hydrodynamic sizes were found to be 41nm (31nm@2000), 38 nm (31nm@5000) and 46 nm (31nm@20 000). The exceptional hydrodynamic size of 31nm@2000 can be ascribed to instability induced by enhanced inter-particle magnetic attraction with increased particle size. As a result, the short chain of 2000 Da mPEG cannot provide sufficient repulsive force against the magnetic dipole–dipole attraction, resulting in slight agglomeration and large hydrodynamic size. The colloidal stability of mPEG coated nanoparticles was further tested in 0.9% NaCl and PBS solution. Fig. 7a shows the optical images of a typical 19nm@2000 sample dispersed in water, 0.9% NaCl, and PBS solution. No observable aggregation in salt and PBS could be seen in these images. The zeta potential *versus* pH for the 19nm@2000 was measured and shown in Fig. 7b. The results suggest an isoelectric point at approximately pH 5.2. In physiological environment with a pH value of about 7.4, the surface charge of nanoparticles of ~23 mV could provide electrostatic repulsion to confer colloidal stability. In fact, the dispersions in 0.9% NaCl or PBS have been stored at 4 °C for 6 months without any observable aggregation. The variation of the hydrodynamic size of 19 nm and 31 nm Fe_3O_4 nanoparticles with different mPEG coatings over a period of 10 days are presented in Fig. 7 c and d. It was found that all of the 9nm and 19 nm samples coated by mPEG with different chain lengths retained their initial hydrodynamic size even after 10 days. Such excellent stability of these nanoparticle dispersions renders them suitable for biomedical applications *in vivo*. However, for the samples with large particle sizes like 31nm@5000 and 31nm@20 000, the hydrodynamic size was observed to be stable for only 5 days. In particular, 31nm@2000 showed signs of aggregation after just 2 days, which again proves that the mPEG2000 coating could not stabilize the 31 nm Fe_3O_4 nanoparticles. As the stability of MFH is indispensable for high performance hyperthermia treatments, the selection of an appropriate surface coating and corresponding magnetic core size is of paramount importance. The results from these stability tests clearly shows that the dispersion of 31 nm Fe_3O_4 nanoparticles exhibits poor colloidal stability even with 20 000 Da mPEG coating, while both 9 nm and 19 nm Fe_3O_4 nanoparticles could form very stable dispersions in both water and simulated physiological conditions.

Table 1 The mean hydrodynamic diameters of different mPEG coated Fe_3O_4 nanoparticles

Surface coating	9 nm Fe_3O_4	19 nm Fe_3O_4	31nm Fe_3O_4
mPEG2000	18 nm	25 nm	41 nm
mPEG5000	21 nm	29 nm	38 nm
mPEG20 000	27 nm	35 nm	47 nm

SAR measurements

In order to evaluate the effect of the mPEG coating of the Fe_3O_4 nanoparticles on hyperthermia applications, the magnetic heating characterization was carried out using an induction heating system (Ambrell, Easy Heat,4.2–10 kW). Fig. 8a shows the experimental setup for calorimetric measurements. In all

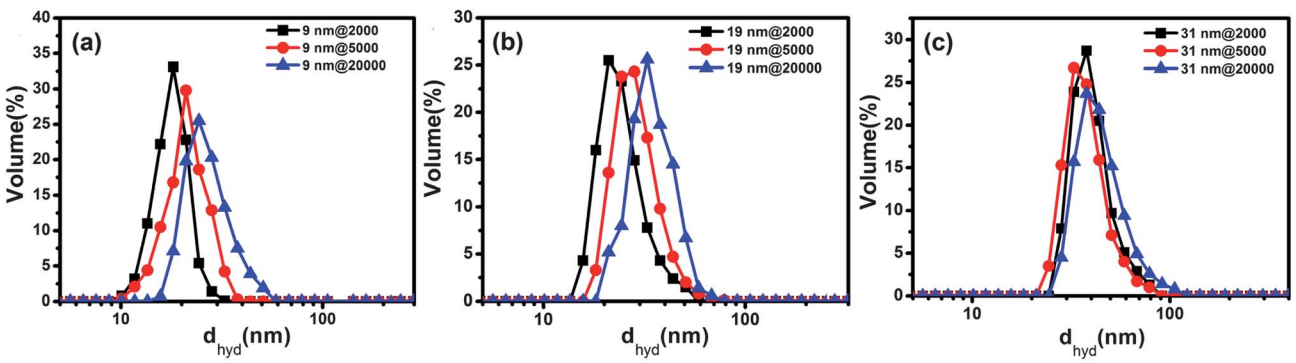

Fig. 6 Hydrodynamic diameters of the mPEG coated Fe_3O_4 nanoparticles in water. (a) 9 nm Fe_3O_4 nanoparticles, (b) 19 nm Fe_3O_4 nanoparticles, and (c) 31 nm Fe_3O_4 nanoparticles.

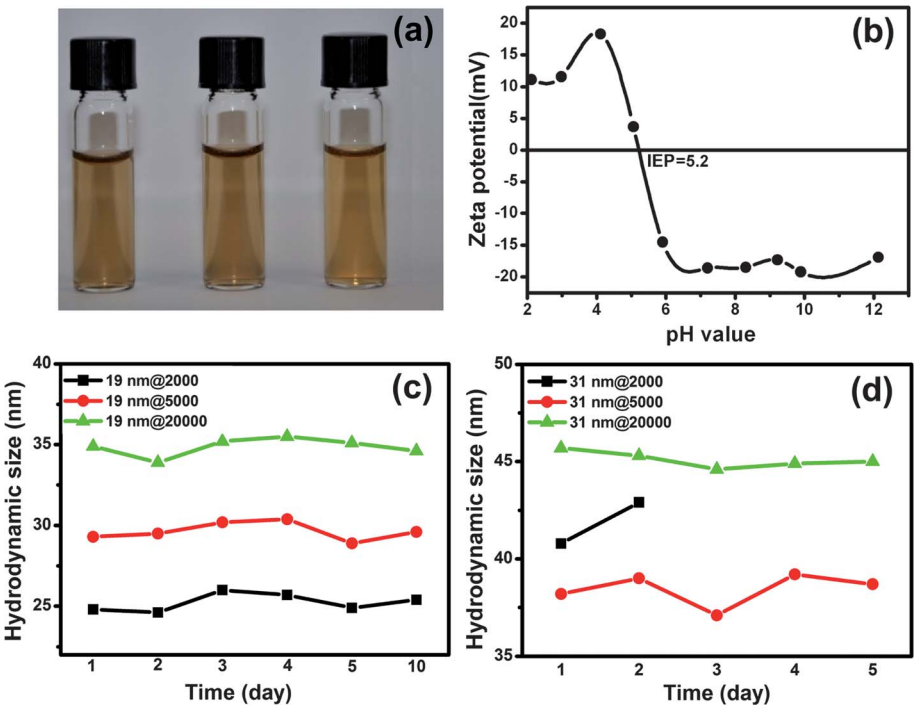

Fig. 7 (a) Digital photographs of 19 nm Fe_3O_4 nanoparticles in water (left), in 0.9% NaCl (center) and in pH 7.4 PBS solution (right). (b) Zeta potential measurements of 19 nm Fe_3O_4 nanoparticles in aqueous solution. (c) and (d) Time dependent hydrodynamic size of 19 nm and 31 nm Fe_3O_4 nanoparticles coated with different mPEG, respectively.

measurements, 1 ml of aqueous Fe_3O_4 nanoparticles dispersion was used and subjected to an AMF (27 kA m^{-1}, 400 kHz). Temperature changes were then recorded using a fiber thermocouple. Fig. 8b shows that the times required to raise the temperature to 42 °C are approximately 481 s for 9nm@2000, 485 s for 9nm@5000, and >600 s for 9nm@20 000. This observation clearly shows that the rate of temperature rise increases with decreasing polymer chain length. Similar phenomenon is

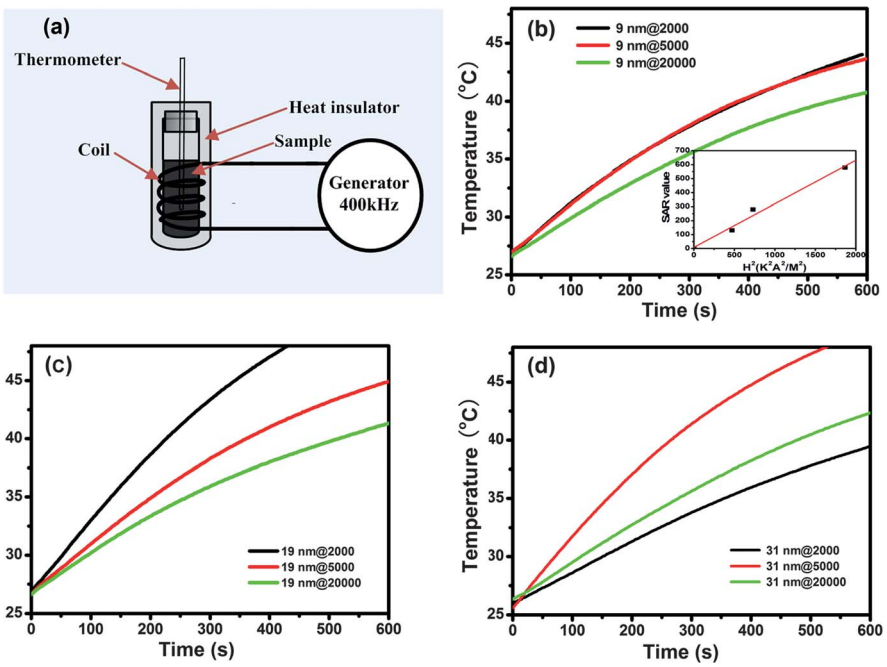

Fig. 8 (a) Experimental setup for calorimetric measurements. Time dependent heating profiles of 1 ml Fe_3O_4 nanoparticles of sizes: (b) 9 nm, (c) 19 nm, and (d) 31 nm coated with different mPEG on exposure to 27 kA m^{-1} alternating current field at 400 kHz frequency. Inset of (b) shows field-dependent specific absorption rate values of 1 ml sample with 0.5 mg ml^{-1} iron concentration.

found for 19 nm samples as shown in Fig. 8c. The inset of Fig. 8b illustrates the field-dependent SAR values of the 9nm@2000 particles with 0.5 mg mL^{-1} iron concentration at 400 kHz frequency. The linear relationship between the SAR and H^2 is in good agreement with both early reports and the theoretical equation mentioned above.[23,44] However, anomalous behavior was observed for the 31 nm Fe_3O_4 samples. As shown in Fig. 8d, the heating rate of 31nm@5000 is higher than that of 31nm@2000. In addition, the heating rate of 19nm@2000 is also higher than the 31nm@2000 at the same Fe concentration, despite the fact that the 31nm@2000 sample has a larger particle size and M_s. We believe that such anomalous behavior is due to the poor colloidal stability of 31nm@2000 that results in partial agglomeration upon application of an external AMF.

The measured SAR values of Fe_3O_4 nanoparticles with different coatings are presented in Fig. 9a. Fig. 9b shows a schematic diagram of magnetic cores with different mPEG coatings. As seen in Fig. 9a, the 19 nm samples consistently exhibits a higher SAR than the 9 nm samples with the same coating thickness due to increased magnetic core size and M_s. The maximum SAR is 930 W g^{-1} achieved by 19nm@2000 sample. In addition, the SAR was observed to decrease with increasing polymer chain length for both the 9 nm and 19 nm samples. As for the 31 nm samples, the SAR of 31nm@5000 is higher than that of 31nm@2000 as a result of the agglomeration of 31nm@2000, but reduces with a further increase in polymer chain length (*i.e.*31nm@20 000). To better understand the relationship between the coating thickness and SAR, here we define δ as the approximate thickness of polymer coating, where δ = hydrodynamic size – magnetic core size (TEM observation). For the sake of comparison, the detailed SAR, δ and M_s of the different samples are shown in Table 2. It was found that the largest SAR for a certain sized sample is the one with the smallest thickness. For the smaller 9 nm samples, the SAR increases by only 37% when the molecule weights of coating polymer changed from 20 000 Da to 2000 Da. However, a significant increase of SAR (74%) is observed for 19 nm samples with the same change of molecular weight. The variation of SAR for the 31 nm samples is about 56% when the molecular weights decrease from 20 000 Da to 5000 Da, while the SAR of the 19 nm nanoparticles under same conditions increases by 28%. It should be noted that the 31nm@2000 sample is not comparable in this case as it is unstable under AMF. These data reveal that a significant enhancement of the SAR is favorable for larger nanoparticles at the same variation of coating thickness, in other words, the polymer coating is more effective in altering the SAR of larger particles than small particles.

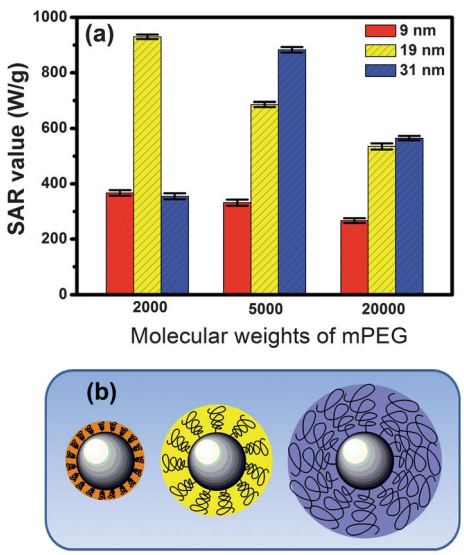

Fig. 9 (a) The SAR values of the different sized Fe_3O_4 nanoparticles for different mPEG: 9 nm (orange), 19 nm (yellow), 31nm (blue). (b) A schematic diagram of nanoparticle based hyperthermia agents with iron oxide core and varied mPEG coating.

Table 2 The comparison of SAR, saturation magnetization (M_s) and coating thickness (δ) of different mPEG coated Fe_3O_4 nanoparticle samples

Samples	Coating Thickness δ/nm	M_s/emu g^{-1}	SAR/W g^{-1}
9nm@2000	9	51	367 ± 10
9nm@5000	12	49	332 ± 11
9nm@20 000	18	46	267 ± 9
19nm@2000	6	59	930 ± 8
19nm@5000	10	57	686 ± 9
19nm@20 000	16	54	535 ± 11
31nm@2000	10	63	355 ± 11
31nm@5000	7	63	883 ± 10
31nm@20 000	16	62	565 ± 8

For the nanoparticle based hyperthermia agent comprising of a magnetic core and a surface coating, the surface coating could strongly affect the processes of Brownian–Néel relaxation and thermal conductivity upon application of an AMF. In principle, it has three main contributions on the measured SAR. First, the surface coating stabilizes the nanoparticles and results in a magnetic colloid system with good dispersibility. The larger sized nanoparticles required mPEG of a higher molecular weight to achieve stable dispersion and high SAR, as verified by the 31 nm Fe_3O_4 nanoparticles. Second, surface coating largely affects the Brownian relaxation loss as indicated in eqn (4). Earlier experimental evidence has shown that the Brownian loss could contribute to ~53% of the total heating capacity for finite sized magnetite nanoparticle dispersion.[43] In extreme cases, the Brownian movement of the particles might be hindered due to a dense and thick coating layer, grossly reducing the SAR. Since the Brownian mechanism has a significant contribution in large sized particles because of the relative higher magnetic anisotropy, the surface coating would have much more effect on large magnetic particles than smaller ones. This is consistent with our observations that with decreasing mPEG chain length, a large enhancement in the SAR was observed for the large particles. It is also worth noting that the polymer coating could affect the medium viscosity in highly concentrated dispersions, leading to a change in the SAR. However, since the concentration of Fe_3O_4 nanoparticle dispersions used in this work was quite low, the contribution from the possible change of viscosity is negligible. Third, the induction heat generated by the magnetic core would be subjected to heat conduction loss due to indirect contact with water. The heat conduction of the surface coating follows Fourier's law and is described as $H = kA\ \Delta T/x$, where k is the conduction coefficient, A is the total cross sectional area of

conducting surface, ΔT is the temperature difference, and x is the thickness of surface coating. Accordingly, a thicker surface coating would result in a decreased SAR, which is in good agreement with our results. In addition, a highly hydrophilic polymer is preferred because it, to some extent, could construct direct contact between magnetic core and the surrounding water, resulting in a high SAR. The mPEG coated Fe_3O_4 nanoparticles provide a model system to study the mechanism of optimization of surface coating for high performance hyperthermia agent. As demonstrated, the SAR could be effectively tuned by the rational design and optimization of the surface coating for a certain magnetic core.

Apart from the optimization of the physical and chemical properties of the surface coating for high performance SAR, the physiological characteristics of the surface coating must also be considered for biomedical applications. Further induction heating tests of optimized 19nm@2000 dispersions were carried out using simulated physiological environments consisting of protein (BSA), blood sugar (glucose), electrolytes (saline), and PBS (pH 7.4), respectively. Normal glucose levels in human blood are about 80 mg per 100 mL before meals and about 120 mg per 100 mL after meals.[45] Fig. 10a shows the SAR values of 19nm@2000 in glucose solutions with the glucose concentration up to 1000 mg L^{-1}. The SAR values for all of the samples are between 901 and 938 W g^{-1}, which is close to the measured SAR value in pure water (930 W g^{-1}). The magnetic nanoparticles could even achieve a SAR of 924 W g^{-1} at high glucose concentrations of 1000 mg L^{-1}, suggesting that glucose did not interact with the mPEG coated Fe_3O_4 nanoparticles. In human blood, serum proteins and lipoproteins are the most abundant proteins. Fig. 10b shows the SAR values obtained in BSA solution with the concentrations of 0–10%. All measured SAR values are in the range of 903–930 W g^{-1}, no significant difference in the SAR value was observed in the range of BSA concentrations used. Similar high SAR values for saline solutions with different NaCl concentrations and PBS were also observed as shown in Fig. 10 c and d. Though further *in vivo* study is necessary in the future, these results imply that the 19nm@2000 dispersion could maintain their high heating capacity in various physiological environments and thus has great potential to be used in biomedical applications as a high performance MFH agent.

Conclusion

In summary, highly monodispersed mPEG coated Fe_3O_4 nanoparticles were used as a model system to investigate the effects of the surface coating on the SAR under an AMF (400 KHz). Investigations of different factors such as particle size, magnetic properties of the magnetic core and surface coating have explicitly shown that by fine-tuning the surface coating for an optimal magnetic core size, the SAR could be significantly increased by up to 74% with a very small variation on the saturation magnetization (<5%). Enhanced SAR with decreasing thickness of surface coating was observed, which was ascribed to the increased Brownian loss and improved thermal conductivity. In addition, large particles with high M_s were favored for high SAR values, however, subsequently increased interparticle attraction tended to reduce the colloid stability and SAR values. Increasing the coating thickness could confer colloidal stability and improve the SAR for large particles as demonstrated in the case of 31 nm sample, however further increases to the coating

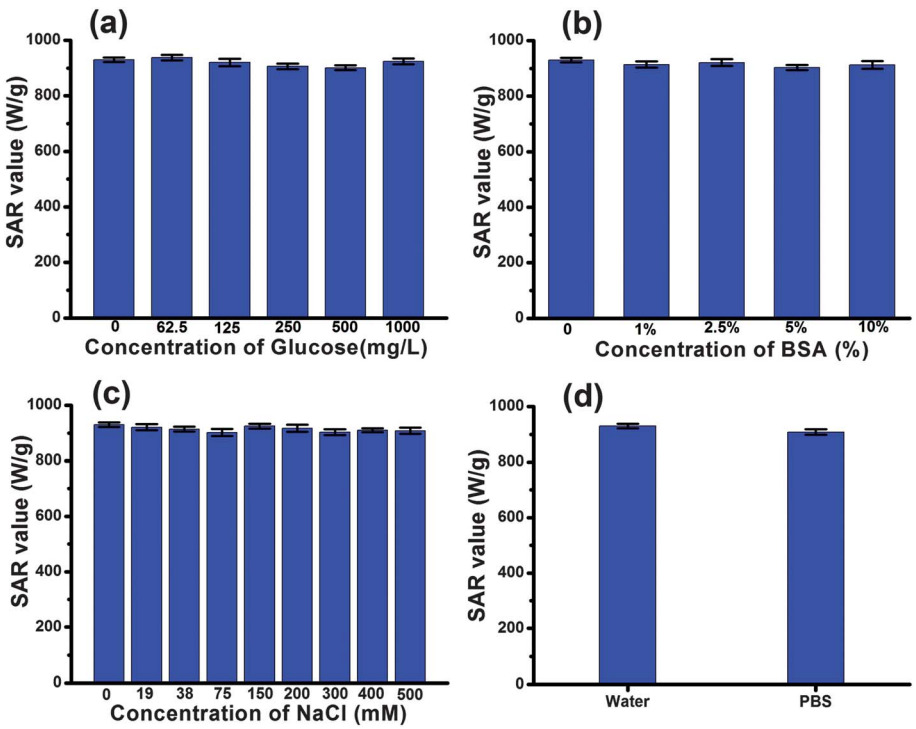

Fig. 10 SAR values for 19nm@2000 samples in different simulated solutions (a) glucose; (b) BSA; (c) NaCl solution; and (d) PBS. The heating capacity for all samples of Fe_3O_4 nanoparticles with concentration of 0.5 mg mL^{-1} were performed under an AMF with a frequency of 400 KHz.

thickness led to a decrease in the Brownian loss and thermal conductivity, leading to a poor SAR. Therefore, by elaborate optimization of both surface coating and particle size, 19nm@2000 exhibited the highest SAR of 930 W g^{-1} among these samples. Moreover, this hyperthermia agent with optimized surface coating has shown excellent performance in both water and simulated physiological conditions. Such an optimization of surface coating of magnetic nanoparticles based hyperthermia agent is an indispensable step towards practical biomedical applications. The findings obtained in this work provide a general strategy for the optimization of biocompatible surface coatings for the design and development of novel magnetic nanoparticle-based hyperthermia agents for advanced nano-biotechnology applications.

Acknowledgements

This work was financially supported by the National Natural Science Foundation of China (Grant No. 21006079) and MOE AcRF Tier 2 -MOE2011-T2-1-043.

Notes and references

1 Y. M. Huh, Y. W. Jun, H. T. Song, S. Kim, J. S. Choi, J. H. Lee, S. Yoon, K. S. Kim, J. S. Shin and J. Cheon, *J. Am. Chem. Soc.*, 2005, **127**, 12387.
2 F. Y. Cheng, C. H. Su, Y. S. Yang, C. S. Yeh, C. Y. Tsai, C. L. Wu, M. T. Wu and D. B. Shieh, *Biomaterials*, 2005, **26**, 729.
3 Y. W. Jun, Y. M. Huh, J. S. Choi, H. J. Lee, H. T. Song, S. Kim, S. Yoon, K. S. Kim, J. S. Shin, J. S. Suh and J. Cheon, *J. Am. Chem. Soc.*, 2005, **127**, 5732–5733.
4 N. Nasongkla, E. Bey, C. Khemtong, J. S. Guthi, S. F. Chin, A. D. Sherry, D. A. Boothman and J. Gao, *Nano Lett.*, 2006, **6**, 2427–2430.
5 H. M. Fan, M. Olivo, B. Shuter, J. B. Yi, R. Bhuvaneswari, H. R. Tan, G. C. Xing, C. T. Ng, L. Liu and J. Ding, *J. Am. Chem. Soc.*, 2010, **132**, 14803–14811.
6 O. B. Miguel, M. P. Morales, P. Tartaj, J. R. Cabello, P. Bonville, M. Santos, X. Zhao and S. V. Veredagner, *Biomaterials*, 2005, **26**, 5695.
7 S. Mornet, S. Vasseur, F. Grasset and E. Duguet, *J. Mater. Chem.*, 2004, **14**, 2161.
8 P. J. Chen, S. H. Hu, C. S. Hsiao, Y. Y. Chen, D. M. Liu and S. Y. Chen, *J. Mater. Chem.*, 2011, **21**, 2535.
9 A. Jordan, P. Wust, H. Fahling, W. John, A. Hinz and R. Felix, *Int. J. Hyperthermia*, 1993, **9**, 51–68.
10 R. Hergt, S. Dutz, R. Müller and M. Zeisberger, *J. Phys.: Condens. Matter*, 2006, **18**, S2919–S2934.
11 J. P. Fortin, *J. Am. Chem. Soc.*, 2007, **129**, 2628–2635.
12 R. E. Rosensweig, *J. Magn. Magn. Mater.*, 2002, **252**, 370–374.
13 A. Jordan, R. Scholz, P. Wust and H. Schirra, *J. Magn. Magn. Mater.*, 1999, **194**, 185.
14 A. K. Gupta and M. Gupta, *Biomaterials*, 2005, **26**(18), 3995–4021.
15 S. Mornet, S. Vasseur, F. Grasset and E. Duguet, *J. Mater. Chem.*, 2004, **14**, 2161–2175.
16 Z. H. Lu, M. D. Poruty and Z. H. Gao, *Langmuir*, 2005, **21**, 2042–2050.
17 M. Ma, Y. Wu, J. Zhou, Y. K. Sun and Y. Zhang, *J. Magn. Magn. Mater.*, 2004, **268**, 33–39.
18 L. A. Thomas, L. Dekker, M. Kallumadil, P. Southern, M. Wilson, S. P. Nair, Q. A. Pankhurstc and I. P. Parkin, *J. Mater. Chem.*, 2009, **19**, 6529–6535.
19 A. A. El-Gendy, E. M. M. Ibrahim, V. O. Khavrus, S. Hampel, A. Leonhardt, B. Büchner and R. Klingeler, *Carbon*, 2009, **47**, 2821–2828.
20 D. L. Zhao, X. W. Zeng, Q. S. Xia and J. T. Tang, *J. Alloys Compd.*, 2009, **469**, 215–218.
21 A. Demortiere, P. Panissod, B. P. Pichon, G. Pourroy, D. Guillon, B. Donnio and S. Begin-Colin, *Nanoscale*, 2011, **3**, 225.
22 R. Hergt, R. Hiergeist and M. Zeisberger, *J. Magn. Magn. Mater.*, 2005, **293**, 80.
23 R. Hergt, R. Hiergeist and M. Zeisberger, *et al.*, *J. Magn. Magn. Mater.*, 2004, **280**, 358.
24 A. P. Khandhar, R. M. Ferguson and K. M. Krishnan, *J. Appl. Phys.*, 2011, **109**, 07B310.
25 J. H. Lee, J. T. Jang, J. S. Choi and J. W. Cheon, *Nat. Nanotechnol.*, 2011, **6**, 418.
26 S. Tong, S. Hou, Z. Zheng, J. Zhou and G. Bao, *Nano Lett.*, 2010, **10**, 4607–4613.
27 E. Amstad, T. Gillich, I. Bilecka, M. Textor and E. Reimhult, *Nano Lett.*, 2009, **9**, 4042.
28 (*a*) L. Li, Y. Yang, J. Ding and J. M. Xue, *Chem. Mater.*, 2010, **22**, 3183–3191; (*b*) J. Park, K. An, Y. Hwang, J. G. Park, H. J. Noh, J.-Y. Kim, J.-H. Park, N.-M. Hwang and T. Hyeon, *Nat. Mater.*, 2004, **3**, 891–895; (*c*) S. Sun, H. Zeng, D. B. Robinson, S. Raoux, P. M. Rice, S. X. Wang and G. Li, *J. Am. Chem. Soc.*, 2004, **126**, 273–279.
29 U. I. Tromsdorf, O. T. Bruns, S. C. Salmen, U. Beisiegel and H. Weller, *Nano Lett.*, 2009, **9**, 4434.
30 B. A. Bornstein, P. S. Zouranjian, J. L. Hansen, S. M. Fraser, L. A. Gelwan, B. A. Teicher and G. K. Svensson, *Int. J. Radiat. Oncol., Biol., Phys.*, 1993, **25**, 79–85.
31 D. Maity, P. Chandrasekharan, J. M. Xue, J. Ding and S. S. Feng, *Nanomedicine*, 2010, **5**(10), 1571–1584.
32 H. M. Fan, G. J. You, Y. Li, Z. Zheng, H. R. Tan, Z. X. Shen, S. H. Tang and Y. P. Feng, *J. Phys. Chem. C*, 2009, **113**, 9928–9935.
33 Y. Zeng and S. M. Zhou, *Electrochem. Commun.*, 1999, **1**(6), 217.
34 T. Özkaya, M. S. Toprak, A. Baykal, H. Kavas, Y. Köseoglu and B. Aktas, *J. Alloys Compd.*, 2009, **472**, 18.
35 L. Zhang, R. He and H. Gu, *Appl. Surf. Sci.*, 2006, **253**, 2611.
36 C. Barrera, A. P. Herrera and C. Rinaldi, *J. Colloid Interface Sci.*, 2009, **329**, 107–113.
37 X. Y. Li, X. Y. Kong and Z. Y. Qian, *Carbohydr. Polym.*, 2010, **79**, 429–436.
38 E. Karaǒglua, A. Baykala, H. Deligözb, M. S,enela, H. Sözeric and M. S. Toprakd, *J. Alloys Compd.*, 2011, **509**, 8460–8468.
39 H. Ando, M. Nakahara and M. Yamamoto, *Langmuir*, 1996, **12**, 6399.
40 M. Suzuki, A. Fujisjima, T. Miyazaki, H. Hisamitsu and H. Ando, *J. Biomed. Mater. Res.*, 1997, **37**, 252.
41 O. Iglesias and A. Labarta, *Phys. Rev. B: Condens. Matter*, 2001, **63**, 19.
42 B. Jeyadevan, *J. Ceram. Soc. Jpn.*, 2010, **118**, 391–401.
43 K. Y. Wina and S. S. Feng, *Biomaterials*, 2005, **26**, 2713–2722.
44 L. L. Lao and R. V. Ramanujan, *J. Mater. Sci.: Mater. Med.*, 2004, **15**, 1061–1064.
45 S. W. Chen, *J. Magn. Magn. Mater.*, 2010, **322**, 247–252.

